Materials and Design 36 (2012) 348–358

Contents lists available at SciVerse ScienceDirect

Materials and Design

journal homepage: www.elsevier.com/locate/matdes

Finite-element thermal analysis of laser welding of galvanized high-strength steel in a zero-gap lap joint configuration and its experimental verification

Junjie Ma, Fanrong Kong, Radovan Kovacevic *

Center for Laser-Aided Manufacturing, Lyle School of Engineering, Southern Methodist University, 3101 Dyer Street, Dallas, TX 75205, USA

ARTICLE INFO

Article history:
Received 31 August 2011
Accepted 11 November 2011
Available online 26 November 2011

Keywords:
C. Lasers
D. Welding
G. Thermal analysis

ABSTRACT

A three-dimensional (3D) finite element (FE) model is applied to predict the temperature evolution in the laser welding of galvanized high-strength steels in a zero-gap lap joint configuration. A rotary Gaussian volumetric heat source model is introduced to simulate the laser energy input. The temperature data measured by thermocouples are used to verify the boundary conditions of the thermal model. The experimentally verified finite element model is then used to predict the weld pool size and the area of vaporized zinc at the faying surface. A feature parameter that represent the ratio of the zinc coated vaporized area to the area of molten pool at the faying surface has been established. The acquired values of the feature parameters could be used to numerically estimate the weld quality with respect to the different laser welding parameters. A series of tensile shear tests for the lap-jointed DP980 steel coupons has been performed correspondingly. The experimental results show that failure load of lap joint of galvanized DP980 steel increases with a lower welding speed or higher laser power. It is found that there is a potential relationship between the area of vaporized zinc at the faying surface of lap joint of galvanized steel and the final weld quality, and a decrease in the welding speed or increase in laser power mitigates to a certain extent the defects caused by zinc vapor in the weld bead.

1. Introduction

The automobile industry is increasing the usage of novelty steels like galvanized high strength steels in car body manufacturing due to their high corrosion resistance, high strength, and good formability [1]. However, a series of new technical problems has arisen in the laser welding of zinc coated steels in a zero-gap lap joint configuration. The boiling point of zinc is 907 °C, which is significantly lower than the melting point of steel (above 1500 °C). Ribic et al. [2] reported that during the welding process, high pressurized zinc vapor is easily generated at the faying surface and vents out through the weld pool, resulting in blowholes and porosity in the solidified weld bead. A number of experimental techniques have been proposed to mitigate the effect of zinc vapor in the laser welding of galvanized steels in a zero-gap lap joint configuration. One technique is based on applying an appropriate gap between the faying surfaces in order to evacuate the zinc vapor, which has been studied separately by Imhoff et al. [3] and Akhter et al. [4,5]. Another technique is based on redesigning the configuration of the lap joint in order to release the zinc vapor before the steel starts to melt, which has been introduced by Graham et al. [6]. Mazumder et al. [7,8] introduced a thin copper sheet at the interface of lapped sheets in order to form the Zn–Cu alloy before the molten pool reaches the interface. Li et al. [9,10] placed an aluminum foil at the faying surface along the weld line to form the Al–Zn compounds in order to decrease the zinc vapor pressure. Gu and Mueller [11] added the gas tungsten arc welding process as the second heat source to the laser welding of galvanized steels. Kim et al. [12] separated these two heat sources and established a relationship between the weldability and the process parameters in the zero-gap lap-joint configuration. Yang and Kovacevic [13] applied this procedure to weld galvanized dual-phase (DP) high strength 980 steel in a zero-gap lap joint configuration. The experimental study of the specific role of the shielding gas with variable composition on the quality of weld in the laser welding of zero-gap lap-jointed galvanized steel has been presented by Yang et al. [14]. By investigating hybrid laser/GMA welding of galvanized steels in a lap joint configuration, Ribic et al. [2] concluded that a longer solidification time allows the zinc vapor an easier escape from the interface zone of the joint through the liquid phase. Considering an enlarged weld pool has a longer solidification time, a larger weld pool would allow the zinc vapor an easier escape from the pool. However, a larger weld pool means an increase in the area of boiled zinc, the larger area coated by zinc at the faying surface. This issue needs to be further studied.

Because it is time-consuming and expensive to completely depend on laboratory experiments, numerical analysis as a cost-effective way has been adapted to investigate the temperature field in the laser welding process. Mazumder and Steen [15]

* Corresponding author. Tel.: +1 214 768 4865; fax: +1 214 768 0812.
E-mail address: kovacevi@lyle.smu.edu (R. Kovacevic).

0261-3069/$ - see front matter © 2011 Elsevier Ltd. All rights reserved.
doi:10.1016/j.matdes.2011.11.027

developed the numerical model for the continuous laser welding process by assuming a complete laser absorption on the surface when the temperature exceeded the boiling point. Swift-Hook and Gick [16] analytically developed the heat conduction model by treating the laser beam as a moving line heat source. In addition, Dowden et al. [17] developed a model for the keyhole welding under the conditions of a low welding speed. Lankalapalli et al. [18] assumed the keyhole of the conical shape and a two-dimensional heat conduction model was developed to predict the penetration depth of the weld. Goldak et al. [19] proposed a three-dimensional (3D) "double ellipsoid" heat source model based on the real molten pool dimensions, which showed its suitability for modeling the high power density welding processes. A "Gaussian rod" type volumetric heat source was used by Frewin and Scott [20] and Chang and Na [21] in their numerical model; however, the predicted cross-sectional shape of the weld could not match the "nail-head" shape at the weld well. Du et al. [22] presented a combined heat source model consisting of a Gaussian surface heat source and a cylindrical heat source to describe the temperature field of the laser welding. The former heat source is used to simulate the heating effect of the laser-induced plasma, and the latter one is introduced to consider the laser generated keyhole absorption. Wu et al. [23] established a rotary Gaussian volumetric heat source model, showing that they could achieve more accurate simulation of the temperature distribution in the laser welding. It would be very interesting to numerically explain the effect of zinc vapor on the weld quality. Dasgupta et al. [24] developed a 3D numerical model to predict the zinc vaporization in the keyhole on the heat transfer and fluid flow in the CO_2 laser welding of galvanized steel for lap joint configuration. However, the zinc vapor diffusion through the liquid zone of the molten pool has been ignored. Loredo et al. [25] developed a numerical model to optimize the process parameters with the limited number of experimentations during the zinc ablation process in a zero-gap lap joint configuration. However, there are only few similar numerical studies that have taken in consideration the effect of the zinc vapor on the welding of galvanized steel in a zero-gap lap joint configuration.

To better understand the influence of various welding parameters on the temperature distribution during the laser welding of galvanized steels, the numerical method is carried out to predict the area of weld pool and the area of vaporized zinc at the faying surface of lap joint by using a rotary Gaussian volumetric heat source. Here the zinc coating thickness is assumed to be constant. Experiments of laser welding of galvanized steels in a zero-gap lap joint configuration are performed with the measurement of the temperature histories by the thermocouples. The experimentally-verified thermal analysis results are then used to predict the geometry size of weld pool and the vaporized zinc at the faying surface of the lap joint of galvanized steel with different welding speeds and laser powers. A series of experiments has also been performed correspondingly to study the influence of the laser power and the weld speed on the weld quality of DP980 steel in which a high-speed CCD camera, assisted with a green laser as the illumination source, is used to monitor the behavior of the molten pool in real time. The whole simulation is carried out by using ANSYS Parametric Design Language (APDL).

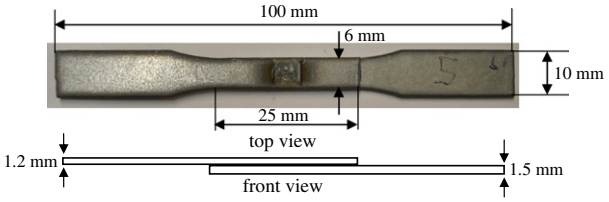

Fig. 2. The specimen for tensile shear test.

2. Experimental setup

A fiber laser of 4 kW in power is used to perform the weld of galvanized steel. The laser welding head has a focused spot of 0.6 mm in diameter. The experimental setup that consists of the fiber laser and a 6-axis high precision robot is shown in Fig. 1. The clamps are used to fix both ends of the coupons. The pure argon is employed as side shielding gas to mitigate the laser-induced plasma and to protect the molten material against corrosion. The gas flow rate is set at 30 standard cubic feet per hour (SCFH). A robotic control panel is used to control the welding path and to implement the welding procedure. A high-speed CCD camera with a frame rate of 4000 per second is used to monitor the behavior of the molten pool in real time, and a green laser with the band pass of 532 nm at wavelength is selected as the illumination source. The base material used in this study is the galvanized high strength DP980 steel. The two-sheet stack-up coupons are cut by an abrasive water-jet cutting system with the dimensions of 72 mm × 46 mm × 1.2 mm and 72 mm × 46 mm × 1.5 mm. The 1.2-mm thick sheet is selected to be the top sheet and the 1.5-mm thick sheet is placed at the bottom. The two metal sheets are then tightly clamped together during the laser welding process, and a zero gap is assumed to be achieved. The thermocouples are installed near the weld area to record the temperature history. Furthermore, the tensile shear tests are carried out to evaluate the

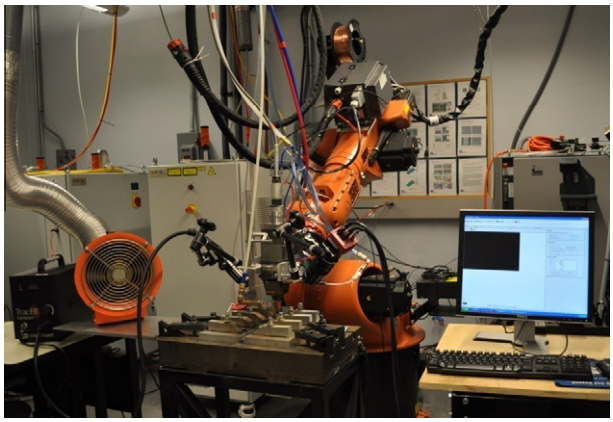

Fig. 1. Experimental setup.

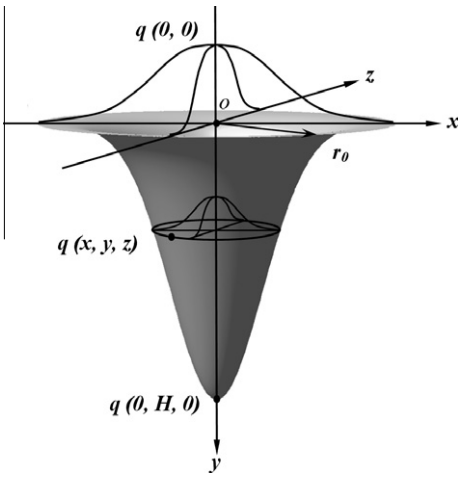

Fig. 3. Schematic of rotary-Gaussian body heat source model [23].

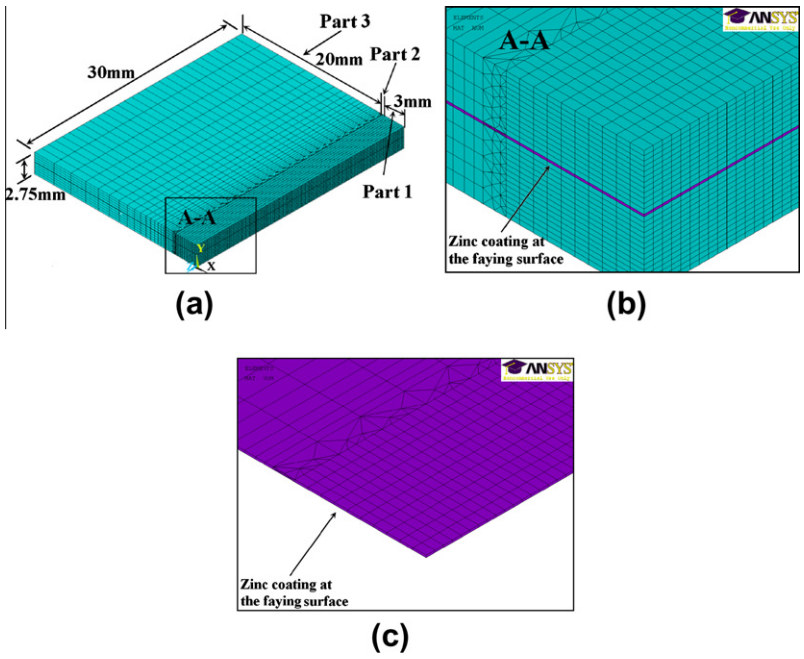

Fig. 4. Schematic view of the dimensions of the meshed coupon: (a) general view, (b) close-up of weld zone, and (c) the zinc coating at the faying surface.

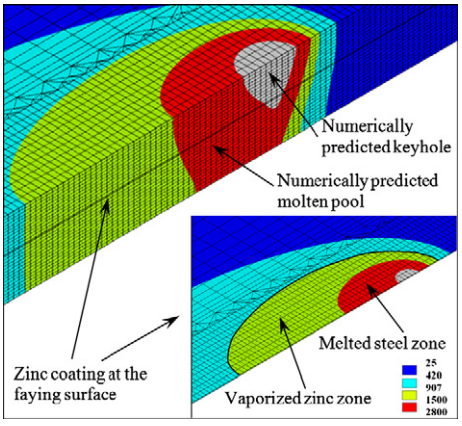

Fig. 5. Schematic view of numerically predicted keyhole and molten pool and heat distribution along the faying surface in FE model.

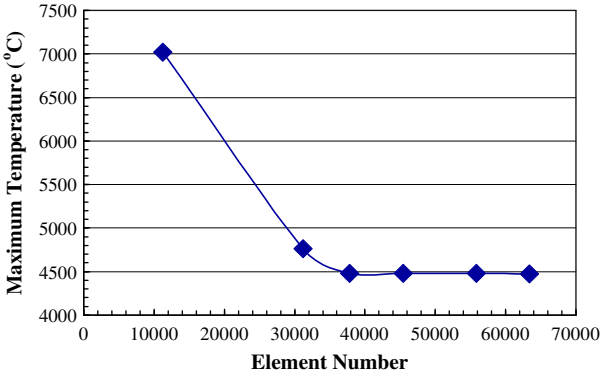

Fig. 6. The mesh convergence parametric study.

strength of the welds. The coupons for testing are cut by the abrasive water jet machine (see Fig. 2). In addition, the coupons with cross-section of the weld bead are polished and etched by standard metallographic procedure in order to perform the metallographic study.

3. Finite element modeling

3.1. Basic assumption

In order to reasonably simplify the finite element thermal analysis of laser welding of galvanized steel sheets in a lap joint configuration, some basic assumptions have been applied as follows:

(1) The fluid flow in the molten pool is ignored.

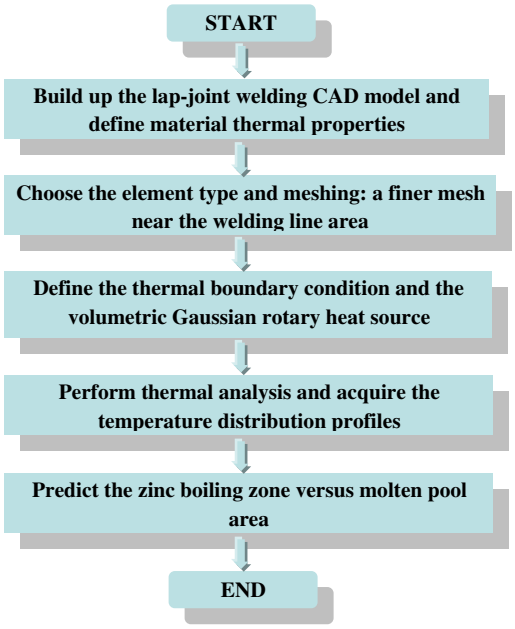

Fig. 7. Flowchart of numerical simulation procedure.

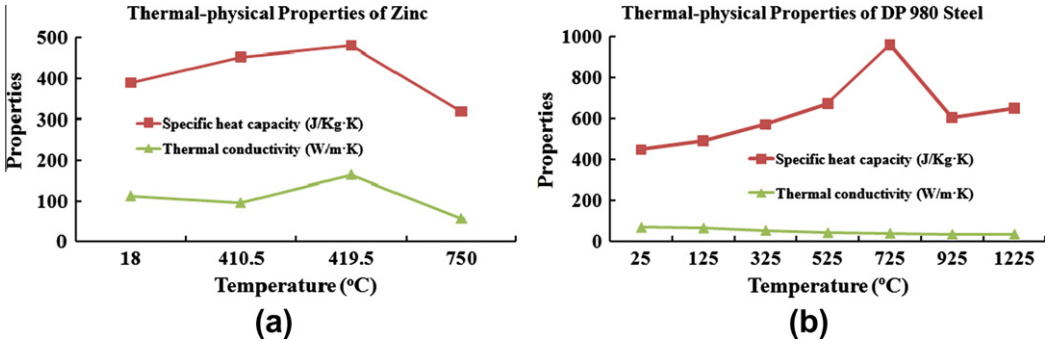

Fig. 8. Thermal-physical properties of (a) Zinc [28] and (b) DP980 steel [29].

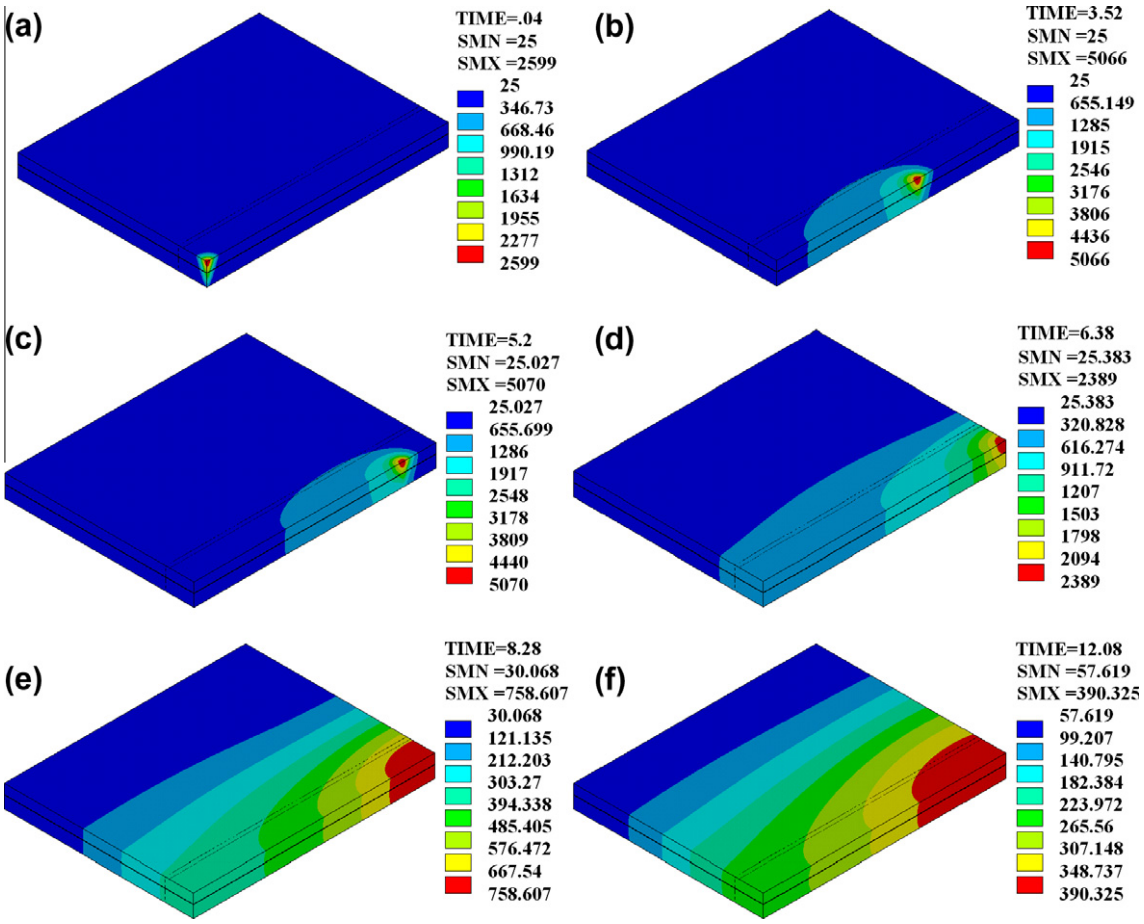

Fig. 9. Temperature contours evolution in the welding process: (a) $t = 0.04$ s, (b) $t = 3.52$ s, and (c) $t = 5.2$ s, and in the cooling phase (d) $t = 6.38$ s, (e) $t = 8.28$ s, and (f) $t = 12.08$ s.

(2) The heat input from laser irradiation obeys a rotary Gaussian volume distribution, which was introduced by Wu et al. [23].
(3) The influence of zinc vapor diffusion on the thermal properties of weld zone is ignored.

3.2. Governing equation

The quasi-steady state temperature field during the laser welding is governed by the following equation:

$$\rho\frac{\partial(c_pT)}{\partial t}=\frac{\partial}{\partial x}\left(k\frac{\partial T}{\partial x}\right)+\frac{\partial}{\partial y}\left(k\frac{\partial T}{\partial y}\right)+\frac{\partial}{\partial z}\left(k\frac{\partial T}{\partial z}\right)+\dot{q}_{\text{laser}} \quad (1)$$

where ρ is the density, c_p is the specific heat, T is temperature, t is time, k is thermal conductivity, and x, y, z, are Cartesian coordinates; $\dot{q}_{\text{laser}}$ is the laser radiation induced volume heat input given by Wu et al. [23] shown in Fig. 3:

$$\dot{q}_{\text{laser}}=\frac{9\eta Q}{\pi H r_0^2(1-e^{-3})}\exp\left(\frac{9(x^2+(z-vt)^2)}{r_0^2\log(\frac{y}{H})}\right) \quad (2)$$

where Q is the nominal power of the laser beam, η is the absorption coefficient, y varies from 0 to H, H is the depth of weld, v is the welding speed, and r_0 is the effective radius of the volumetric heat source on material surface.

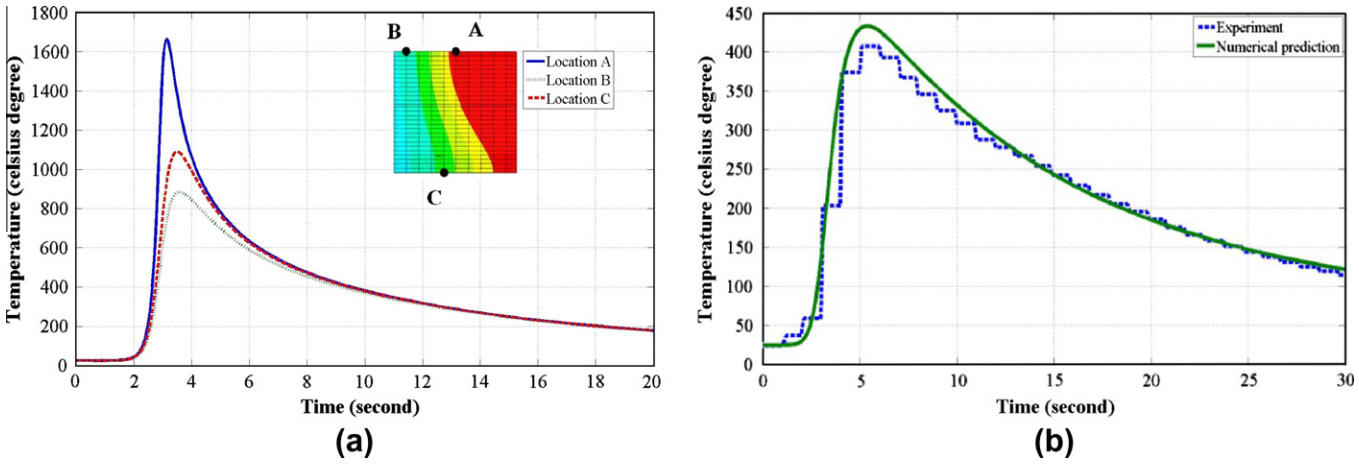

Fig. 10. (a) Temperature evolution at three characteristic locations and (b) the comparison of numerically predicted and experimentally measured temperature at 4.55 mm from the weld center line at the top surface.

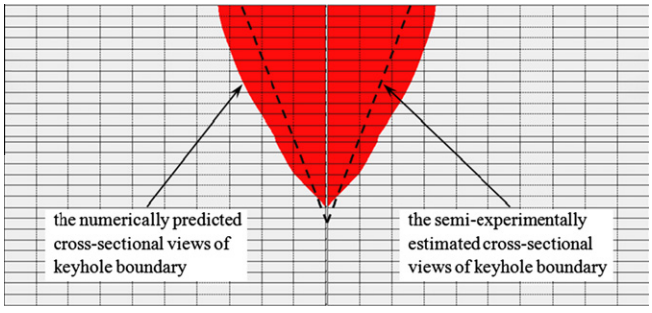

Fig. 11. Comparison of the numerically predicted and semi-experimentally estimated cross-sectional views of keyhole boundary [18,31].

The boundary conditions for thermal analyses are as follows:

$$\text{At the symmetric plane, } \frac{\partial T}{\partial x} = 0 \tag{3}$$

$$\text{At the other work piece surfaces, } -k\left(\frac{\partial T}{\partial n}\right) = \alpha_T (T - T_\infty) \tag{4}$$

where T_∞ is the ambient temperature, α_T is the combined heat transfer coefficient, and n is the normal outward vector to the surface of specimen.

3.3. Numerical procedure implementation

The dimension of the model is shown in Fig. 4a. Only halves of the two welded plates are selected to be modeled by using the symmetry of the geometry and loads. A non-uniform finite element (FE) mesh is used to save computational cost. As shown in Fig. 4b, a dense mesh is used in part 1 to assure a good numerical accuracy, a much coarser mesh is adopted for part 3, and a free mesh is used for part 2 in order to connect the other two parts. Part 1 is meshed with a 20-node hexahedral element (SOLID90), a 10-node tetrahedral element (SOLID87) is used for part 2, and an 8-node hexahedral element (SOLID70) is used for part 3 [26]. As shown in Fig. 4c, the zinc coating at the faying surface is also taken into account in the FE mesh by using the same mesh density as in the neighboring steel zone. The thickness of zinc coating at the steel surfaces is set at 0.025 mm in the FE model.

An APDL based subroutine is written to simulate the melting and vaporizing areas of the metal and zinc coating at the faying surface of two steel sheets respectively. Fig. 5 shows the temperature distribution in the FE model and along the faying surface acquired from the simulation results. From the temperature distribution profile, the isotherms that corresponds of the boiling point (2800 °C) and the melting point (1500 °C) of the DP980 steel denote the keyhole and the melted steel boundary, while the region between the isotherms that represent the zinc boiling point (907 °C) and the steel melting point indicates the vaporized zinc zone.

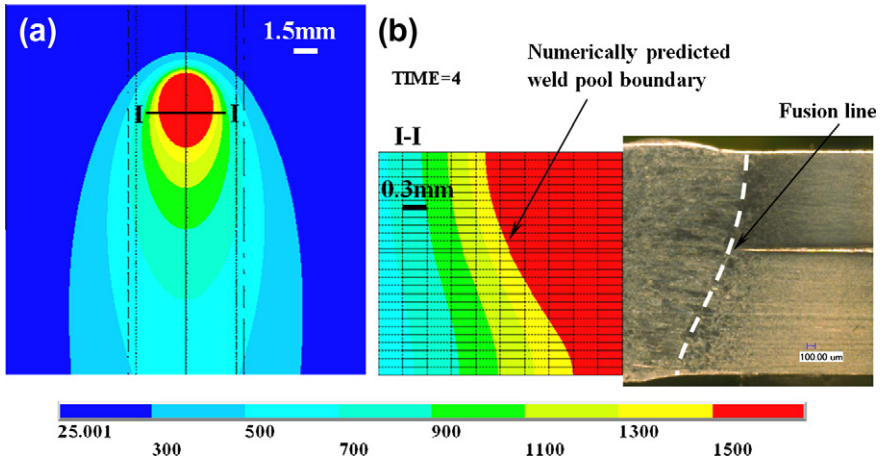

Fig. 12. (a) Numerically predicted heat transfer distribution at the top surface and (b) comparison of the numerically predicted (left side) and experimentally obtained (right side) cross-sectional views of weld bead at the I–I section marked in (a).

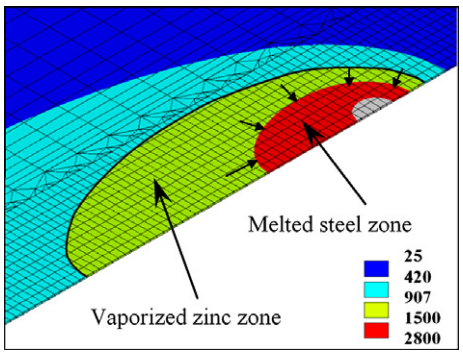

Fig. 13. The schematic view of the zinc vapor escape through the liquid phase of the molten pool at the faying surface.

According to Gross's work presented in the book edited by Dowden [27], the independence of the grid is very important to the accuracy of numerical simulation; however, it is usually ignored. In this study, several levels of meshes (element numbers varying from 10,000 to 70,000 in scales of width, length and depth) are chosen for checking the effect of mesh size on the convergence of computations. A mesh convergence parametric study is carried out. As shown in Fig. 6, the simulated temperature data become independent on the mesh density after 45,000 elements. Thus, a mesh of over 55,000 elements is chosen in this study. Nearby and along the welding line area, the elements at the top and bottom sheets have the dimensions of 0.3 mm × 0.2 mm × 0.1 mm; the elements of the zinc coating at the faying surface have the dimensions of 0.3 mm × 0.2 mm × 0.05 mm.

The simulation procedure is shown in Fig. 7. First, the computer aided design (CAD) model of galvanized steel sheets placed in a zero-gap lap-joint configuration is built by taking the zinc coating into consideration. The density of zinc is 7140 kg/m^3, and the density of DP980 steel is 7842 kg/m^3, while the thermal conductivity, k, and the specific heat capacity, c_p, are temperature dependent which are presented by Yang's dissertation [28] and American Galvanizers Association [29] as shown in Fig. 8. Considering that a high temperature gradient is located at the welding area, a finer mesh is chosen near and inside the weld zone. Then the thermal boundary conditions, and the rotary Gaussian volumetric heat source model, are defined to simulate the temperature profiles. Based on the simulation results, the area of the zinc boiling zone versus the molten pool area can be acquired.

4. Results and discussion

4.1. Temperature field of laser welding of galvanized steel

The Gaussian rotary heat source is used to simulate the temperature field in laser welding of galvanized steel in a zero-gap lap-joint configuration. The welding parameters are selected as follows: the laser power Q is 1.4 kW, according to Kawahito et al. [30] the absorption coefficient η is 0.88, the effective radius of the volumetric heat source on material surface r_0 is 1.25 mm, the welding speed v is 5 mm/s, and the pure argon is chosen as side shielding gas and set at the flow rate of 30 SCFH. Fig. 9a–f shows the temperature distribution in the welded samples at different instances. SMN and SMX correspond to the minimum and maximum temperature acquired in the simulation results respectively. The peak temperature which is beyond the steel boiling point (2800 °C) is defined as keyhole area. It can be shown that a higher temperature gradient is located at the welding line. During the cooling phase, the temperature of the weld zone is gradually reduced until reaching room temperature.

The temperature histories of three marked characteristic locations (A, B, and C) are shown in Fig. 10a. Fig. 10b shows the comparison of the numerically modeled temperature distribution with respect to the measured temperature by thermocouples at the point located at 4.55 mm from the weld center line at the top

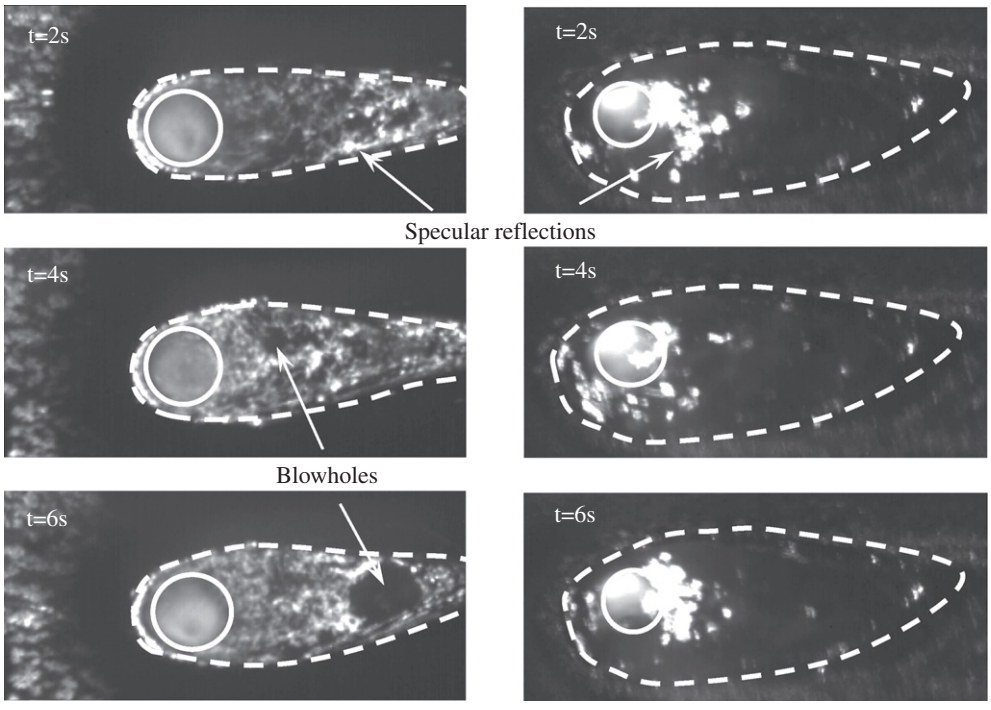

Fig. 14. The dynamic behavior of the molten pool acquired under different welding parameters: (a) laser power of 4.0 kW, welding speed of 30 mm/s, and (b) laser power of 2.0 kW, welding speed of 5 mm/s at different time steps during the welding process.

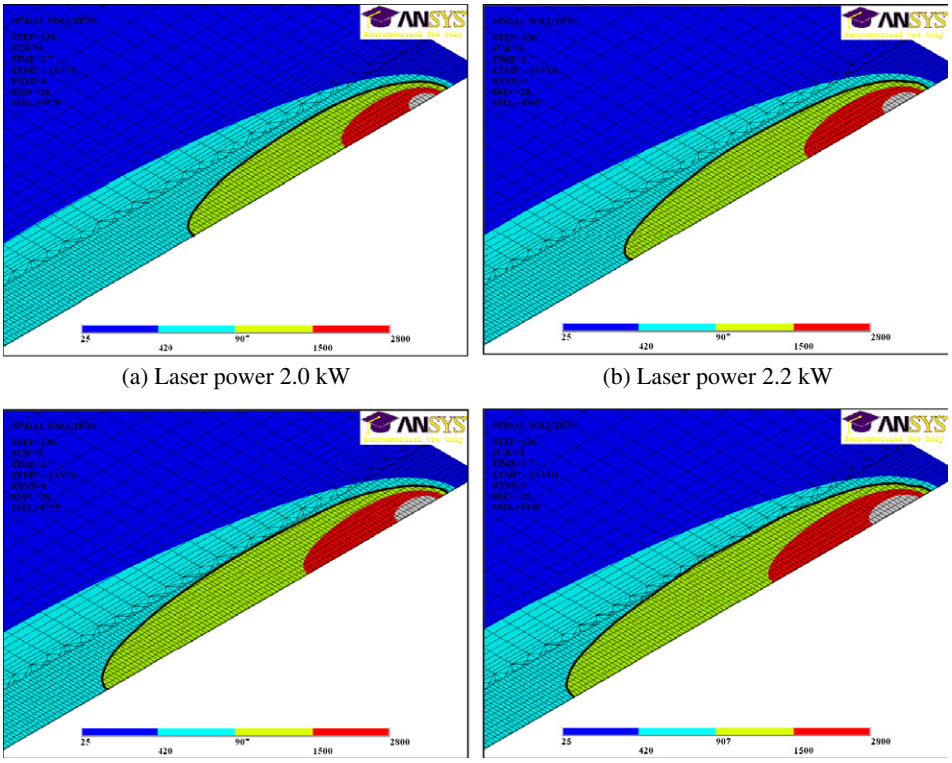

Fig. 15. The vaporized zinc area versus steel melted area at the faying surface with different laser powers (welding speed: 10 mm/s).

surface. It is shown that there is a good agreement between the numerically predicted and experimentally measured results.

Fig. 11 shows the comparison of the numerically predicted cross-sectional views of keyhole boundary and semi-experimentally estimated cross-sectional views of keyhole. The numerically predicted keyhole boundary is defined by the isotherm at the DP980 steel boiling point. The numerically predicted result is verified by a semi-experimental model-based estimation through Eqs. (5)–(7) based on the work of Lankalapalli et al. [18] and Moraitis and Labeas [31].

$$\frac{w}{r} + \beta_1 \exp(-\lambda_1 Pe) + \beta_2 \exp(-\lambda_2 Pe) + \beta_3 \exp(-\lambda_3 Pe) \tag{5}$$

$$r = \frac{2\alpha Pe}{v} \tag{6}$$

$$d = \frac{\eta Q}{\kappa(T_v - T_0)} \frac{1}{(C_1 + (\frac{c_2}{2})Pe + (\frac{c_3}{3})Pe^2 + (\frac{c_4}{4})Pe^3)} \tag{7}$$

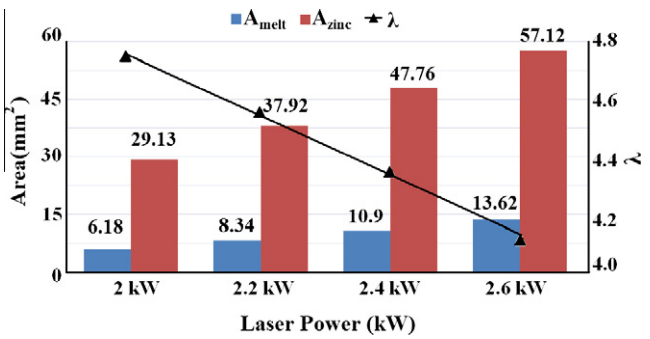

Fig. 16. Effect of the laser power on λ.

where d is the keyhole depth, Q is the nominal power of the laser beam, η is the absorption coefficient, T_v is the boiling temperature of DP 980, T_0 is the ambient temperate, w is the weld pool width, κ is the thermal conductivity, α is the thermal diffusivity, r is the keyhole radius, v is the welding speed, c is the constant independent with material, β and λ are constants related to materials. Here, Q = 1400 W, η = 0.88, T_v = 2800 °C, T_0 = 25 °C, w = 3.3 mm, κ = 65.3 W cm^{-1} °C^{-1}, α = 0.05 cm^2 s^{-1}, v = 5 mm s^{-1}. From Eqs. (5)–(7), the Pe is found to be 0.374, and then the semi-experimentally estimated keyhole depth d is 2.03 mm, the semi-experimentally estimated keyhole radius r is 0.748 mm.

Fig. 12a shows the temperature distribution at the top surface, where the boundary of the molten pool is defined by the isotherm representing the temperature of 1500 °C. Fig. 12b shows the comparison of the isotherms across the cross-section of the weld bead

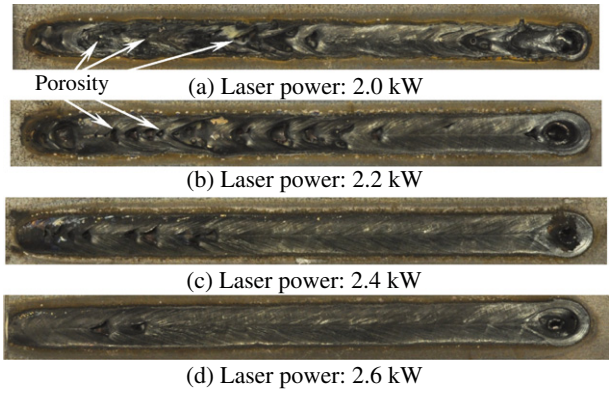

Fig. 17. Top view of the welds under different laser powers (welding speed: 10 mm/s).

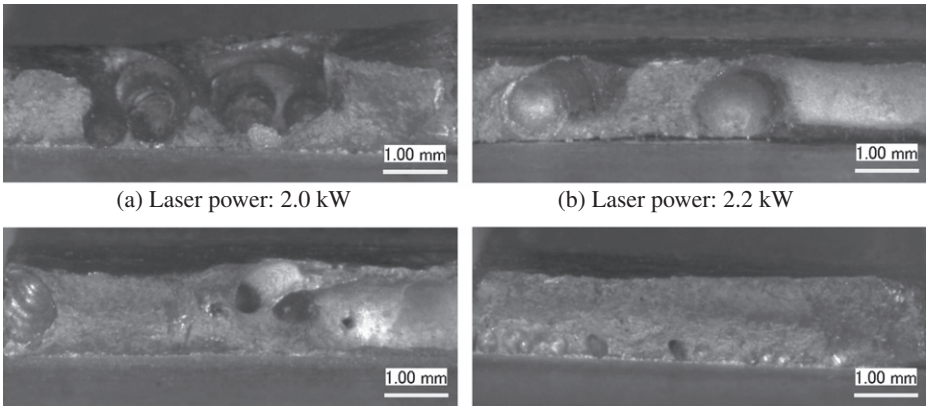

(a) Laser power: 2.0 kW (b) Laser power: 2.2 kW

(c) Laser power: 2.4 kW (d) Laser power: 2.6 kW

Fig. 18. Micrographs of fracture section of weld of lap-jointed galvanized DP980 coupons under different laser powers (welding speed is set at 10 mm/s).

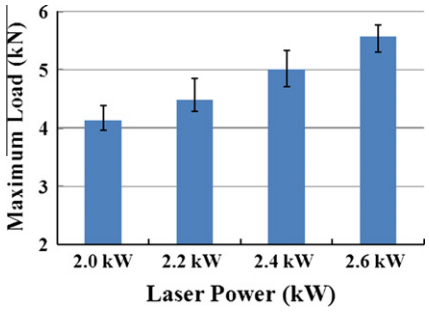

Fig. 19. The failure load versus laser powers for tensile shear testing of lap-jointed galvanized DP980 coupons (welding speed is set at 10 mm/s).

obtained by numerical simulation (left side) with respect to the heat marks across the cross-section of the weld bead (right side). It is evident that there is a good agreement between these two sets of results.

4.2. Prediction of vaporized zinc area at the faying surface and its relationship to weld quality

As shown in Fig. 13, due to the isotherm of zinc boiling point (907 °C), the highly-pressured zinc vapor is generated around the molten pool. When welding of galvanized steels in a zero-gap lap joint configuration, the zinc vapor will not have a direct way to escape, but vent into the liquid phase zone of the molten pool, resulting in the spatters and blowholes. During solidification, the surface

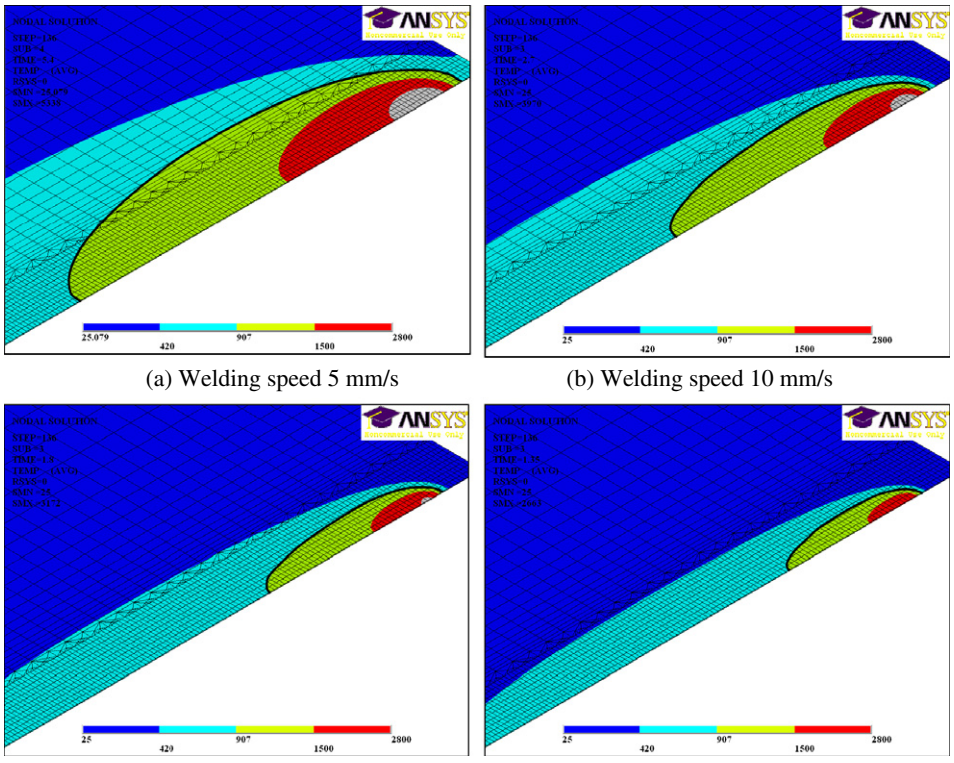

(a) Welding speed 5 mm/s (b) Welding speed 10 mm/s

(c) Welding speed 15 mm/s (d) Welding speed 20 mm/s

Fig. 20. The vaporized zinc area versus steel melted area at the faying surface with different welding speeds (laser power: 2.0 kW).

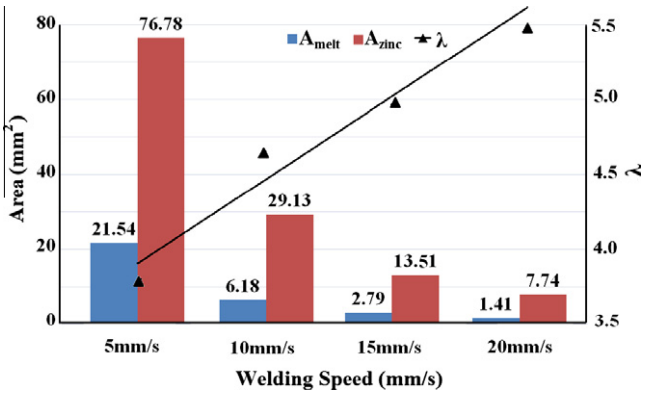

Fig. 21. Effect of the welding speed on λ.

tension of the liquid steel increases, and the blowholes cannot be closed [32].

As shown in Fig. 14, the dynamic behavior of the large and small molten pool at different time during the welding process are acquired under different welding parameters. Due to the readily generating zinc vapor and its escape through the molten pool, a sever fluctuation in the size of the molten pool is shown and the blowholes are formed (see Fig. 14a). However, the enlarged molten pool, Fig. 14b, shows more stability. As mentioned previously [2], the enlarged weld pool has a longer solidification time which would allow the zinc vapor an easier escape.

However, on the other hand, a larger weld pool means an increase in the area of boiled zinc. The larger amount of the vaporized zinc escaping through the weld pool, the easier the spatters and blowholes are generated. Both the quantity of the zinc vapor escaping through the molten pool and the size of the molten pool will affect the weld quality. Therefore, a feature parameter (λ) is introduced in this study to describe the quantity of the zinc vapor escaping through the molten material at the faying surface. Assuming that the zinc coating thickness is constant, the feature parameter (λ) could be represented by the ratio between the zinc coated vaporized area (A_{zinc}) to the molten pool area (A_{melt}) at the faying surface:

$$\lambda = A_{zinc}/A_{melt} \tag{8}$$

The larger the λ is, the larger amount of the zinc vapor escaping through the weld pool is, and the easier the spatters and blowholes are generated. Therefore, the numerically acquired λ value could be used to estimate the weld quality with respect to different laser welding parameters. In order to investigate the relationship between λ and the weld quality, two simulations are carried out. One case is studied to investigate the effect of laser power on the λ, and the other case is performed to investigate the effect of welding speed on the λ. The verification experiments for these two cases are carried out under the same laser power and welding speed as used for the simulation analysis.

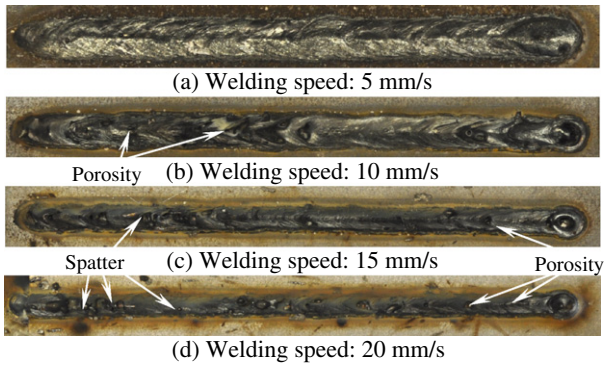

Fig. 22. Top view of the welds under different welding speeds (Laser power: 2.0 kW).

In the first case, the laser power is selected to be 2.0 kW, 2.2 kW, 2.4 kW, and 2.6 kW, respectively, while the welding speed is set at 10 mm/s. Fig. 15 shows the zinc-coated vaporized area and the steel weld pool area obtained by the numerical model described earlier. When the laser power increases, both areas increase but with different ratios of increase, resulting in a decrease of the feature parameter (λ) (Fig. 16). It means, although the absolute amount of the vaporized zinc increased, the amount of the zinc vapor escaping through the molten pool at the faying surface decreases with the increase in the laser power.

At the same time, it could be found from the experimental results (as shown in Fig. 17) that the porosity in the welds decreases (Fig. 17a–d); because the amount of the zinc vapor escaping through the molten pool at the faying surface decreases with the increase in the laser power. Resulting in less zinc vapor trapped in the molten pool during welding process. Thus, the surface quality of the weld improves with the laser power increase. The corresponding tensile shear test results (as shown in Figs. 18 and 19) indicate that the internal pores decrease at the fracture section and the failure loads of the welding joint increase. The quality of weld is definitely improved with an increase in the laser power when the welding speed is kept constant (10 mm/s).

In the second case, the welding speed is selected to be 5 mm/s, 10 mm/s, 15 mm/s, and 20 mm/s, respectively; while, the laser power is set at 2.0 kW. Fig. 20 shows, that with an increase in welding speed, the areas of the boiled zinc and the molten pool decrease with the different rates of change. There is a linear relationship between the change in these areas and the welding speed. As a result, the feature parameter (λ) increases with an increase in the welding speed (Fig. 21), which means an increase in the amount of the zinc vapor escaping through the molten pool at the faying surface. The surface quality of the welds obtained under different welding speeds at a constant laser power suggests that the welding speed of 5 mm/s provides an acceptable weld surface quality (shown in Fig. 22). Because the weld pool formed under this relatively low welding speed (around 5 mm/s) has an enlarged size and a sufficient solidification time will allow the zinc vapor to escape through it. The probability that the zinc vapor will be trapped in the molten pool is obviously decreased. Moreover, it can be seen from the fracture section that the internal pores increase with an increase in the welding speed at a constant laser power (shown in Fig. 23). The results of the tensile shear test of the welds obtained by different welding speeds at the constant power of laser suggests that the tensile shear strength of the DP980 welding joint increases when the welding speed decreases (shown in Fig. 24). However, according to the studies of Karlsson and Kaplan [33], if the welding speed is exceedingly low, the other kind of weld defect like sagging is possible to generate, which also needs to be avoided in the welding process.

It could be concluded that the effect of the zinc vapor on the quality of weld could be controlled by increasing the size of molten pool and decreasing the quantity of zinc vapor or the area of zinc coating that is heated up to the zinc boiling temperature along the faying surface. The λ parameter is verified to be a good indicator for the optimization of the laser welding processing parameters such as the laser power and the welding speed. In general, it should be concluded that the lower value of the λ parameter, means a decrease in the amount of the zinc vapor escaping through the molten pool, resulting in a better weld quality or less porosity in the weld generated by the trapped zinc vapor.

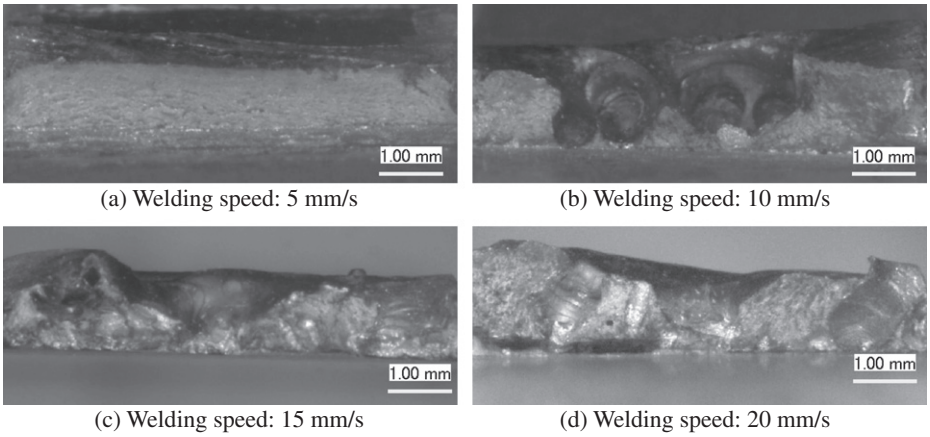

(a) Welding speed: 5 mm/s (b) Welding speed: 10 mm/s

(c) Welding speed: 15 mm/s (d) Welding speed: 20 mm/s

Fig. 23. Micrographs of fracture section of weld of lap-jointed galvanized DP980 coupons under different welding speed (laser power is set at 2.0 kW).

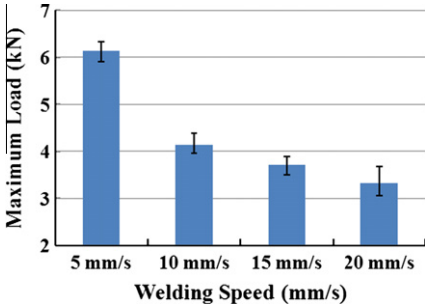

Fig. 24. The failure load versus welding speeds for tensile shear testing of lap-jointed galvanized DP980 coupons (laser power is set at 2.0 kW).

5. Conclusions

An experimentally-based thermal FE model could be used to predict the geometry of the keyhole and the area of the weld pool in the laser welding of galvanized high strength steel DP980 in a zero-gap lap joint configuration, in which a rotary Gaussian volume heat source distribution model is used to simulate the laser energy input. There is a relationship between the ratio of the boiled zinc area and the area of molten pool along the faying surface of lap joint and the final weld surface quality. A feature parameter which represents the amount of the zinc vapor escaping through the molten pool at the faying surface is introduced to represent the quality of weld with respect to the laser welding parameters. The results show that a lower welding speed or higher laser power can mitigate or reduce the weld defects in the weld zone caused by the pressurized zinc vapor. A lower welding speed or higher laser power can definitely mitigate the porosities in the welds thus can consequently elevate the failure loads of the lap-jointed galvanized DP980 coupons.

Acknowledgements

The financial support by NSF's Grant No. IIP-1034652 is acknowledged. The authors would like to thank Mr. Andrew Socha, research engineer; Dr. Shanglu Yang, research engineer; and Dr. Xianfen Li, visiting scholar at Research Center for Advanced Manufacturing at Southern Methodist University for their assistance in performing the experiments.

References

[1] Lagneborg R. New steels and steel applications for vehicles. Mater Des 1991;12(1):3–14.
[2] Ribic B, Palmer TA, DebRoy T. Problems and issues in laser-arc hybrid welding. Int Mater Rev 2009;54(4):223–44.
[3] Imhoff R, Behler K, Gatzweiler W, Beyer E. Laser beam welding in car body making. In: Proceedings of the 5th international conference on lasers in manufacturing. Stuttgart, West Germany, September 13–14; 1988.
[4] Akhter R, Steen WM, Cruciani D. Laser welding of zinc-coated steel. In: Proceedings of the 5th international conference on lasers in manufacturing. Stuttgart, West Germany, September 13–14; 1988.
[5] Akhter R, Steen WM, Watkins KG. Welding zinc-coated steel with a laser and the properties of the weldment. J Laser Appl 1991;3(2):9–20.
[6] Graham MP, Hirak DM, Kerr HW, Weckman DC. Nd: YAG laser beam welding of coated sheet steels using a modified lap joint geometry. Weld J 1996;75(5):162–70.
[7] Dasgupta A, Mazumder J, Bembenk M. Alloying based laser welding of galvanized steel. In: Proceedings of international conference on applications of lasers and electro optics. Dearborn MI; 2000.
[8] Mazumder J, Dasgupta A, Bembenk M. Alloy based laser welding; 2002. US patent 6,479,168.
[9] Li X, Lawson S, Zhou Y. Novel technique for laser lap welding of zinc coated sheet steels. J Laser Appl 2007;19(4):259–64.
[10] Li X, Lawson S, Zhou Y. Lap welding of steel articles having a corrosion resisting metallic coating; 2008. US Patent No. 2008/0035615 Al.
[11] Gu H, Mueller R. Hybrid welding of galvanized steel sheet 20th International congress on applications of lasers & electro-optics. ICALEO; 2001. p. 130–9.
[12] Kim C, Choi W, Kim J, Rhee S. Relationship between the welding ability and the process parameters for laser-TIG hybrid welding of galvanized steel sheets. Mater Trans 2008;49(1):179–86.
[13] Yang S, Kovacevic R. Welding of galvanized dual-phase 980 steel in a zero-gap lap joint configuration. Weld J 2009;88(8):168–78.
[14] Yang S, Carlson B, Kovacevic R. Laser welding of high-strength galvanized steels in a zero-gap lap joint configuration under different shielding conditions. Weld J 2011;90:8s–18s.
[15] Mazumder J, Steen WM. Heat transfer model for CW laser material processing. J Appl Phys 1980;51:941–7.
[16] Swift-Hook DT, Gick AEF. Penetration welding with lasers. Weld J 1973;52:492–9.
[17] Dowden J, Davis M, Kapadia P. Some aspects of the fluid dynamics of laser welding. J Fluid Mech 1983;126:123–46.
[18] Lankalapalli KN, Tu JF, Gartner M. A model for estimating penetration depth of laser welding processes. J Appl Phys 1996;29:1831–41.
[19] Goldak J, Chakravarti A, Bibby M. A finite element model for welding heat sources. Metall Trans B 1984;15B:299–305.
[20] Frewin MR, Scott DA. Finite element model of pulsed laser welding. Weld J 1999;78:15–22.
[21] Chang WS, Na SJ. A study on the prediction of the laser weld shape with varying heat source equations and the thermal distortion of a sma11 structure in micro-joining. J Mater Process Technol 2002;120(1–3):208–14.
[22] Du H, Hu L, Wang D, Shun C. Simulation of temperature and velocity field during laser keyhole welding. Trans China Weld Inst 2005;26:65–9.
[23] Wu S, Zhao H, Wang Y, Zhang X. A new heat source model in numerical simulation of high energy beam welding. Trans China Weld Inst 2004;25:91–4.
[24] Dasgupta AK, Mazumder J, Li P. Physics of zinc vaporization and plasma absorption during CO2 laser welding. J Appl Phys 2007;102:053108.
[25] Loredo A, Martin B, Andrzejewski H, Grevey D. Numerical support for laser welding of zinc-coated sheets process development. Appl Surf Sci 2002;195(1–4):297–303.
[26] ANSYS Inc., ANSYS 11.0 Manual; 2007.

[27] Dowden J, editor, The theory of laser materials processing: heat and mass transfer in modern technology. 2nd ed.; 2009.
[28] Yang S. May 16, Hybrid laser-arc welding of galvanized high strength steels in a zero-gap lap-joint configuration. Ph.D. Dissertation, Southern Methodist University; 2009.
[29] American galvanizers association. Zinc metal properties; 2008. [retrieved 15.02.09].
[30] Kawahito Y, Matsumoto N, Abe Y, Katayama S. Relationship of laser absorption to keyhole behavior in high power fiber laser welding of stainless steel and aluminum alloy. J Mater Process Technol 2011;211:1563–8.
[31] Moraitis GA, Labeas GN. Residual stress and distortion calculation of laser beam welding for aluminum lap joints. J Mater Process Technol 2008;198(1–3):260–9.
[32] Schmidt M, Otto A, Kägeler C. Analysis of YAG laser lap-welding of zinc coated steel sheets. CIRP Ann – Manuf Technol 2008;57(1):213–6.
[33] Karlsson J, Kaplan A. Fibre laser welding for lightweight design. In: ICALEO 28 conference. Orlando, Florida, USA; 2009.